photonics

MDPI

Communication

A Case Report on Skin Sebum Extraction Using High Lateral Resolution Spectral-Domain Optical Coherence Tomography

Jannat Amrin Luna [1], Sm Abu Saleah [1], Hyunmo Kim [1], Dongwan Kang [1], Daewoon Seong [1], Yoonseok Kim [1], Hayoung Kim [1], Ruchire Eranga Wijesinghe [2], Jeehyun Kim [1] and Mansik Jeon [1,*]

[1] School of Electronic and Electrical Engineering, College of IT Engineering, Kyungpook National University, 80, Daehak-ro, Buk-gu, Daegu 41566, Republic of Korea
[2] Department of Materials and Mechanical Technology, Faculty of Technology, University of Sri Jayewardenepura, Pitipana, Homagama 10200, Sri Lanka
* Correspondence: msjeon@knu.ac.kr

Abstract: Pores are the microscopic openings in the skin that emit oils and sweat. Pores can appear larger due to acne, sun damage, or increased sebum production, a waxy and oily substance that causes oily skin. Investigating and extracting sebum from facial pores is essential for treating skin issues as the enlargement of the pores causes higher susceptibility of the skin to microbe aggressions and inflammatory reactions. In this study, we assessed the volumetric size of pores before and after the sebum extraction using spectral domain optical coherence tomography (SD-OCT). To properly estimate the volume of the sebum before and after extraction, multiple cross-sectional OCT images were selected. The area of a single pixel was calculated from the OCT images using the scanning range. Furthermore, an algorithm was developed to use the pixel area to calculate the full volumetric size of the skin pore. This research illustrates the use of a high-resolution microscopic analysis using SD-OCT in dermatological research and can operate as a guideline for future research investigations in evaluating non-destructively wounded tissue analysis, underlying skin biochemistry, and facial statistical approaches in skin parameters for moisturizer treatment.

Keywords: skin sebum extraction; spectral-domain optical coherence tomography (SD-OCT); skin pore volume; skin tissue imaging; OCT cross-sectional images

Citation: Luna, J.A.; Saleah, S.A.; Kim, H.; Kang, D.; Seong, D.; Kim, Y.; Kim, H.; Wijesinghe, R.E.; Kim, J.; Jeon, M. A Case Report on Skin Sebum Extraction Using High Lateral Resolution Spectral-Domain Optical Coherence Tomography. *Photonics* **2023**, *10*, 30. https://doi.org/10.3390/photonics10010030

Received: 30 November 2022
Revised: 23 December 2022
Accepted: 24 December 2022
Published: 27 December 2022

1. Introduction

The sweat glands and hair follicles on the skin's surface have microscopic holes called pores that allow gases and liquids to pass through. Although they are more prevalent on the face, such as the pores on the nose, they are found in any place on the skin with oil glands. Moreover, pores are tiny indentations in the surface of the skin from which sweat and natural oils emerge, such as sebum. The sebaceous glands produce sebum, an oily material that combines with lipids to form a protective coating on the surface of the skin [1]. The main components of sebum are oily materials, including lipids such as glycerides, free fatty acids, wax esters, squalene, cholesterol esters, and cholesterol [2]. The overproduction of sebum can cause acne and other skin conditions, while insufficient production and excretion can lead to rough, dry, and cracked skin [3–5]. There is a common chronic inflammatory condition known as acne vulgaris that affects the pilosebaceous unit, which includes the hair follicle and the sebaceous gland. It is largely characterized by an increase in sebum production, bacterial colonization, and inflammation [6]. When sebum production is excessive, the pore ducts can become clogged and appear larger due to environmental stress, genetic predisposition, or pathological skin disorders [7]. One of the most important aesthetic concerns is the enlarged facial pores, which can become noticeable features and are closely associated with papules, comedones, pustules, and cysts [8]. Apart from the aesthetic issues, larger pores often provide a convenient entrance for dangerous or potentially pathogenic aggressors, resulting in severe inflammatory

responses [9]. The age-related loss of the dermal integrity and perifollicular structural support can cause skin fragility, sagging and enlarged pores along with other factors that may affect the skin pore size, including chronic recurrent acne, sex hormones, and skin care regimens such as inappropriate use of cosmetics, washing habits, and sun exposure. From a practical perspective, cosmetic conditions are neither health-threatening nor associated with significant morbidity. However, they can affect an individual's emotional well-being and are gaining increased attention. Therefore, it is important to know the pore structure before and after the sebum secretion which is one of the most desired targets of skincare.

In order to study the wound healing processes and analyze the skin structure, various monitoring techniques have been used. Mercury intrusion porosimetry, nitrogen adsorption, and atomic force microscopy (AMF) have been successfully employed for the analysis of pores [10–12]. These procedures can only be used on dry samples and they rely on the assumption that all pores have a regular, interconnected geometry. When the scanning tip's size and the pore's size are comparable (AFM), the tip cannot enter the pore and measure the precise diameter [13,14]. To reduce the pore size and improve acne scars and skin texture, some methods are available such as oxybrasion, hydrogen purification, and pathogenic mechanisms of acne in the treatment of acne vulgaris [15–17]. However, these treatments are only suitable for treating dermatological problems. They are not suitable for cosmetology procedures. Thermoporometry is a calorimetric method to analyze the changes in the pore size distribution of skin and it is based on the observation of solid-liquid phase transition in the pores [18]. In this method, the results must be viewed with caution in the solid-liquid phase transition temperature. The result can be significantly affected by the measurement conditions as they cannot be regarded as correct. Electron microscopy techniques, such as scanning and transmission electron microscopy, can be used to obtain information about the pore size but it is impossible to calculate the pore size distribution, pore volume, and surface area [19]. Although optical imaging methods such as reflectance confocal microscopy, fluorescence microscopy, and second harmonic microscopy have been recognized as promising tools for analyzing tissue structural changes [20–22], their narrow penetration depth and constrained field of view are still considered significant difficulties in the monitoring of tissue regions. Additionally, magnetic resonance imaging (MRI) and X-ray microcomputed tomography (micro-CT) can produce tomographic images with a high depth of penetration in three dimensions. However, MRI techniques are constrained by their resolution capabilities and the quality of micro-CT images is heavily influenced by the system settings and the sample preparation.

OCT is a non-ionized optical imaging technology that provides the internal microstructure of materials and biological tissue structures with micrometer resolution and deeper penetration depth compared to conventional microscopy. Therefore, OCT has been recognized as a powerful diagnostic and research tool for imaging biological tissues. OCT is a dynamic cross-sectional and non-invasive imaging technique based on the low-coherence interference technique that can provide high-resolution, three-dimensional (3D) scattering images of microvasculature biological tissues [23,24]. OCT has also been used in biomedical and clinical investigations in dermatology [25], ophthalmology [26], gastroenterology [27], dentistry [28], otorhinolaryngology [29,30], otology [31], and oncology [32]. Furthermore, OCT is diversely used in multidisciplinary fields, such as industrial evaluation [33], agriculture [34,35], and entomology [36,37]. Non-invasive OCT imaging technology facilitates the investigation of the morphology of sweat ducts [38,39], the qualitative morphological analysis of normal skin [25], and the visualizing of the anatomical structures in biological tissues [40]. The images of the objects can be identified more precisely with a better lateral resolution using an objective lens with a high numerical aperture value even though the effective scan depth is shorter. Furthermore, OCT provides morphological information and allows for a non-invasive internal structural visualization without damaging the tissue.

In this study, the whole internal volumetric structure of the skin pore before and after the sebum extraction was calculated using cross-sectional and enface images of the pore by employing a laboratory-customized OCT system. Moreover, a high numerical

aperture (NA) objective lens with a 10x magnification was employed to compute the small internal volume structure in more detail. Furthermore, the quantitative measurements for the inner structures were performed toward the depth direction and volume segmentation was applied to obtain the result. Therefore, the results of this research can be applied as a fundamental structural analysis of the pores before and after the sebum extraction, demonstrating the viability of non-destructive imaging using OCT, which has the advantage of allowing for the internal structures to be observed without compromising the integrity of the tissue sample.

2. Materials and Methods

2.1. Subject Preparation for Imaging

To evaluate the applicability of the system in dermatological studies and clinical practice, a 26-year-old man volunteered to assist with skin pore imaging. The pores were visible on the skin surface and the cross-sectioned images of conspicuous pores were taken from the nose. An acne extruder was utilized to remove the skin pore and OCT images were taken after the sebum extraction.

2.2. OCT System Configuration

Figure 1a shows the schematic diagram and Figure 1b presents the photograph of the developed high lateral resolution SD-OCT system used in this study for sebum imaging. The system consists of a broadband light source (EXS210022-02, SLED, EXALOS, Schlieren, Switzerland) with a bandwidth (full-width at half-maximum) of 50 nm and a central wavelength of 840 nm. The light from the SLED broadband light source was split and sent to the reference and sample arms separately using a 50:50 fiber coupler (TW850R5A2, Thorlabs, Newton, MA, USA). The output power in the sample arm was approximately 6 mW with a flat-top output profile. The lights that were reflected from the sample and the mirror (PF10-03-P01, Thorlabs, Newton, MA, USA), which were positioned at the end of the reference arm, interfered at the fiber coupler before being transferred to a customized designed spectrometer. The raster scanning of the sample was achieved by mounting two galvanometer scanners (GVS002, Thorlabs, Newton, MA, USA) at the sample arm. For the beam expansion, two distinct focusing lenses (AC254-050-B and AC254-100-B, Thorlabs, Newton, MA, USA) were aligned in the sample arm. Additionally, a high numerical aperture (NA = 0.28) objective lens (10× M Plan APO, Edmund Optics, Barrington, IL, USA) was used to increase the lateral resolution of the system. The custom-made spectrometer was developed in a small aluminum case and equipped with an achromatic lens (AC508-100-B, Thorlabs, Newton, MA, USA), a transmission diffraction grating (1800 lines/mm, Wasatch Photonics Inc., Logan, UT, USA), a mirror, and a high-speed CMOS line scan camera with 2048 (H) 2 (V) pixels (spL2048-140 km, Basler, Ahrensburg, Germany) with a pixel size of 10.0 µm × 10.0 µm. The transmission diffraction grating dispersed the incident light according to its wavelengths, which were then focused by a focusing lens onto the line scan camera. The field of view of the used OCT system was 1.33 mm × 1.3 mm, the depth dimension in a 2D image was 0.955 um and the spectral resolution of the used spectrophotometer was 0.729 um. The measured axial and lateral resolutions of this system were 6.2 µm and 2.46 µm, respectively. An approximate refractive index of the human skin tissue was between 1.36 and 1.43 [41,42] and the lateral resolution of the skin sebum was 1.8. The system displayed the OCT B-scan image once every 20 milliseconds in real time at a frame rate of 50 frames per second. To obtain the complete tomographic images for each volume image, a total of 500 B-scan images were obtained which took 10 s. From the data acquisition to displaying the final OCT cross-sectional (B-scan) images, LabVIEW 2017, an integrated software package, was utilized for all the operations. The hardware, software, and technical specifications of the employed OCT system were laboratory customized.

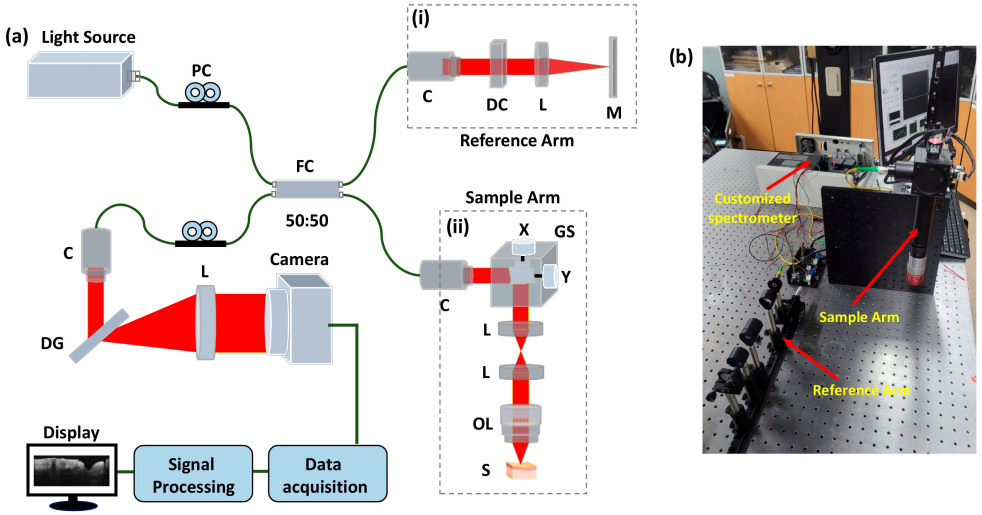

Figure 1. (**a**) Schematic diagram of high lateral resolution spectral-domain optical coherence tomography system and (**b**) a photograph of the used OCT system. C: collimator, DC: dispersion compensation unit, DG: diffraction grating, FC: fiber coupler, GS: galvanometer scanner, L: focusing lens, M: mirror, OL: objective lens, PC: polarization controller, S: sample.

3. Results

3.1. Evaluation of the Cross-Sectional Skin Pore Images with Edge Detection

Figure 2 shows the edge detection process in the skin pore area after the sebum extraction. Figure 2a shows the OCT cross-sectional images of the skin pore after the sebum extraction with a red box in the selected ROI. After loading the OCT cross-sectional image in the MATLAB (R2021a) platform, the noise was filtered out. Following the noise filtering, morphological filtering was carried out to remove the adjacent noise of the hole (after the sebum extraction region) edge, as shown in Figure 2c. In the process of morphological filtering, a grayscale image was processed pixel by pixel based on the values of the adjacent pixels using a square structuring element with a two-pixel width. After the morphological filtering, the image binarization was carried out, as shown in Figure 2d. In this process, a grayscale image was converted to a black-and-white image, reducing the information contained within the image from 256 shades of gray to a binary black-and-white image. All the pixels in the input images with a luminance greater than the predefined threshold value (255) were replaced with the value 1 (white) and all the other pixels were replaced with the value 0 (black). Following the image binarization, the Sobel edge detection technique was applied to the binary image to detect the edge of the hole after extracting the sebum. Figure 2e shows the edge of the sebum-extracted hole, which is marked by the green rectangle. Figure 2f,g shows the extended view of the hole in the cross-sectional images of the original and Sobel edge detected images. By employing this image processing technique, it was possible to identify the significant differences in the image boundaries between the original and processed images.

3.2. Image Processing and Volume Calculation Algorithm

An automatic segmentation system was developed using MATLAB to measure the volume computation procedure before and after the sebum extraction in the skin pore, as shown in Figure 3. The automatic segmentation involved five steps for the volume calculation. The steps were (1) filtering the images, (2) binary masking, (3) thresholding (4) skin pore and hole detection with segmentation, and (5) calculating the final results from the multiple segmented images. First, the original gray-scale OCT image was filtered with the median and gaussian filter to remove the noise. Then the image was converted into binary values and the binary masking was applied to the binary images. The binary mask technique was used to isolate the particular ROI of the OCT images. After that, thresholding

was applied to the binary image. To improve further image processing, thresholding was applied to extract the necessary ROI or the foreground pixels from the background pixels. Following this, the automatic segmentation process was applied to the threshold images using MATLAB. After that, the area of the skin pore and hole was detected before and after the sebum extraction of multiple OCT images. From these multiple images, the total pixel area was estimated. To get the final result, the total internal volume was calculated for the pore and the hole by multiplying the summation of the total area with the total number of the selected images (pore or hole) and the length of each individual image.

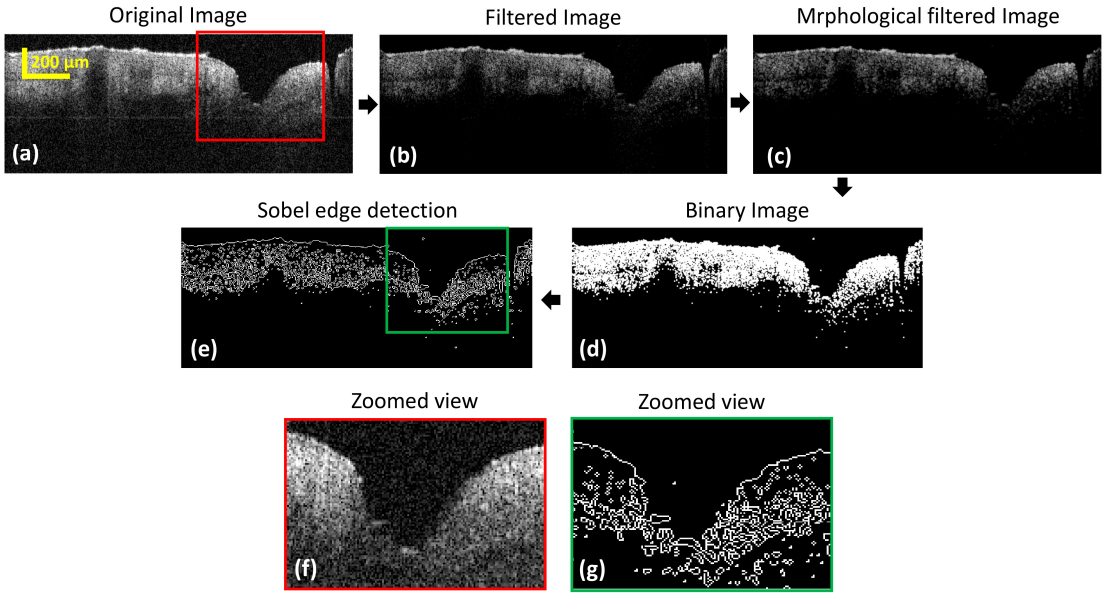

Figure 2. Skin sebum-extracted OCT images with the precise detection of the edges.

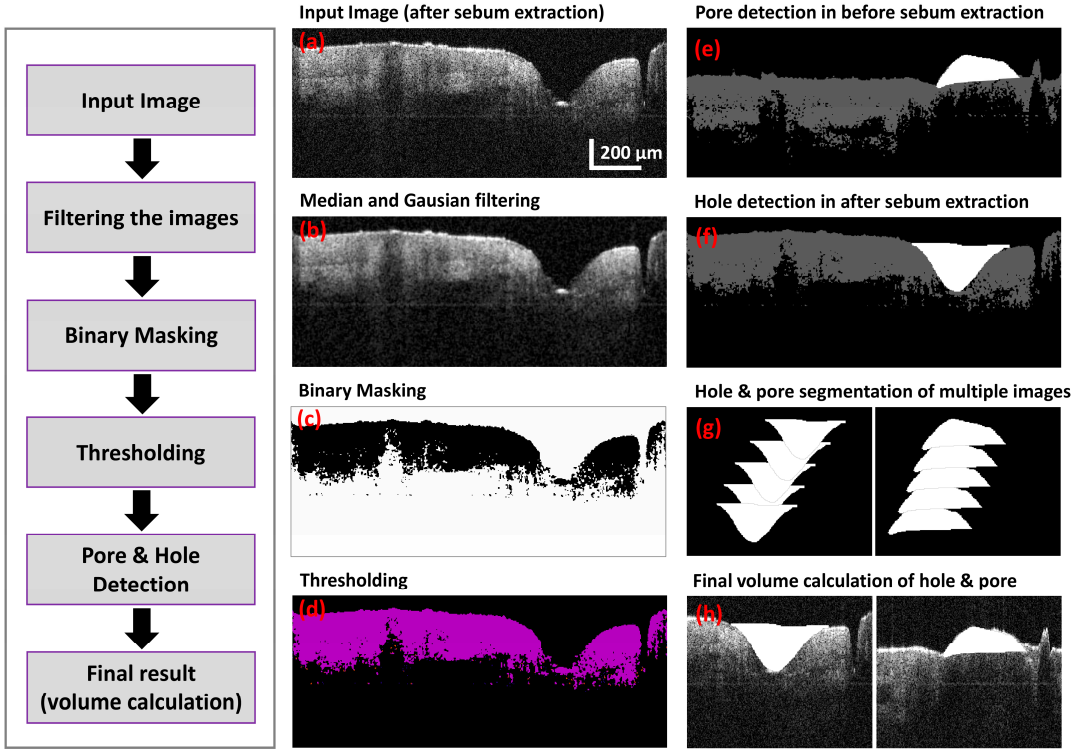

Figure 3. The segmentation algorithm for the quantitative analysis of the volume calculation before and after the sebum extraction.

In order to get the corrected volume, all of the cross-sectional images corresponding to the pore and hole were segmented across the pixels to reconstruct a three-dimensional pore and hole. To observe the quantity of the skin pore and hole, the volume was computed from the pixel area and the findings were quantified and presented for each sebum condition.

3.3. Quantitative Analysis of the 3D Volume of the Skin Pore

Figure 4 depicts the OCT images of the pore before and after the sebum extraction. There were 500 skin pore images before the sebum extraction and 500 images after the sebum extraction, which were used to analyze and calculate the internal volume of a single skin pore. The 2D cross-sectional image and the 3D enface image are shown in Figure 4a,d, and Figure 4b,e before and after the sebum extraction, respectively. The ROI of the skin pore and the hole is indicated in the enface image with a green dotted box in Figure 4b,e, and the 3D view is represented individually in a zoomed visualization in Figure 4c,f. The facial pore is not a fixed structure. It is flexible and may be affected by intrinsic as well as extrinsic factors [43]. The appearance of enlarged facial pores has become a concern and the structural identification of the pore has become an essential requirement in cosmetic fields. The shape, volume, and size distribution affected the pores and, with the 3D representation, the structure of the pore and hole was well-identified. The structure of the pore was apparent on the skin's surface prior to the sebum extraction and the hole region was significantly larger than the pore region, which was located under the skin.

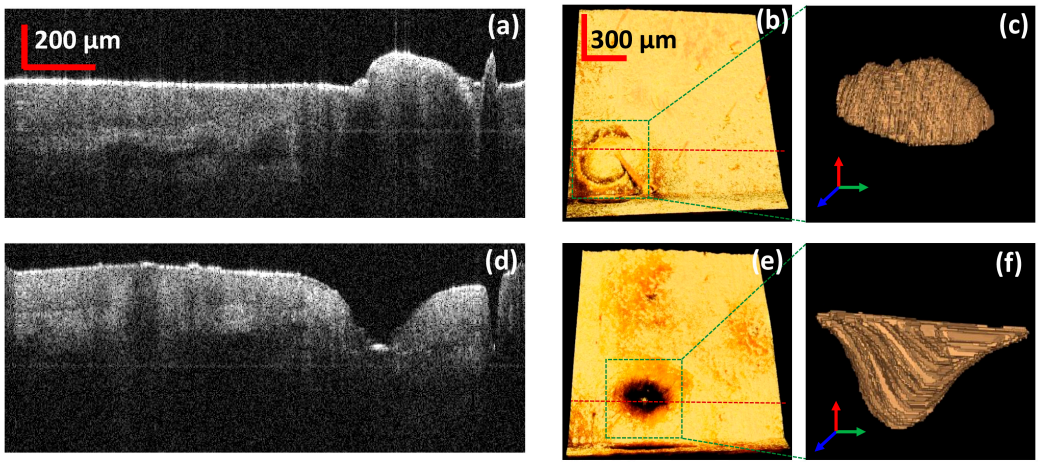

Figure 4. Comparative analysis of the high lateral resolution OCT images before and after the sebum extraction. (**a**,**d**) Cross-sectional OCT images of the sebum region are indicated by the red dotted line in (**b**,**e**); (**b**,**e**) 3D *enface* images; (**c**,**f**) enlarged volumetric ROI indicated by the blue dotted square in (**b**,**e**).

To get accurate volume information and reduce the background noise, 126 and 160 consecutive tomographic images were taken into consideration for the calculation of the skin pore and the hole, respectively. These precise images were taken into consideration since they contained information about the skin pores and holes for the measurement of the volume calculation. At first, the scanning range was used to measure the length and width of a single pixel from the OCT cross-sectional images. After that, the pixel surface area of the individual images (126 and 160) in the specified ROI of the skin pore and the hole was measured using the imageJ software (National Institutes of Health, USA., v-1.53t). Then, the surface area was multiplied by both the total number of B-scan images and the length of each B-scan image.

Figure 5 demonstrates the pixel-by-pixel volume calculation of the selected cross-sectional images. Figure 5a shows the X–Y plane of a single image and the length and width of a single pixel along with a dotted blue line. In Figure 5b, multiple images in the ROI are selected. The calculation of each surface area from each image is represented in

Figure 5c. All the surface areas were summed together to determine the volumetric size of the pore. The volume of the 3D object (skin pore and hole) was calculated, and the volume is represented as a 3D object in Figure 5d.

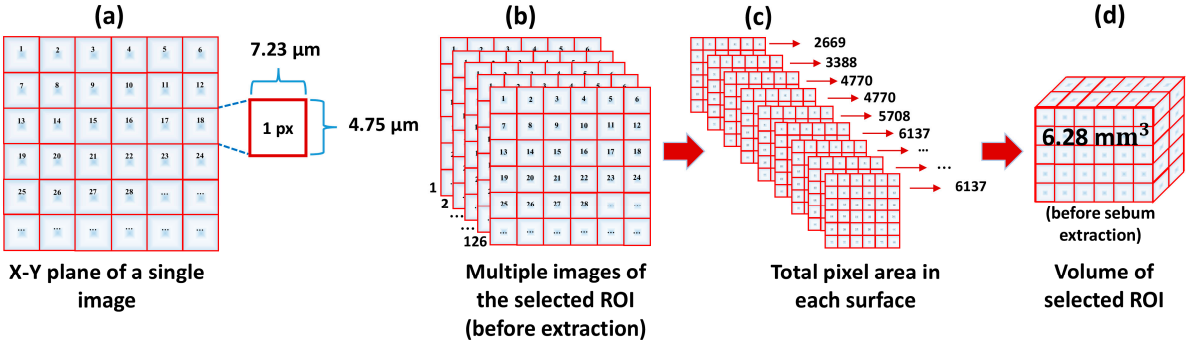

Figure 5. Pixel-by-pixel representation of the volume calculation from the OCT images. (**a**) X-Y plane of a single image; (**b**) selecting multiple images for the calculation of the surface area; (**c**) summation of the surface area from each image plane and (**d**) calculating the volume from the surface area.

The calculated value of the skin pore and hole volume are shown in Table 1. The images used before and after the sebum extraction are 126 and 160, respectively. The volume calculated was 6.28 mm^3 and 9.61 mm^3 for the skin pore and hole, respectively. This evaluation can be useful for analyzing various wound healing processes in addition to the different treatment interventions.

Table 1. Measurement of the total volume before and after the sebum extraction.

Skin Pore Region	Total Area	Total B-Scan	Total Volume	Total Volume	STD±
	um^2	number	um^3	mm^3	mm^3
Before sebum extraction	1.801×10^7	126	6.289×10^9	6.28	0.03
After sebum extraction	2.188×10^7	160	9.699×10^9	9.61	0.02

4. Discussion

In this research, OCT was used to assess the whole internal structure of the facial pore, which is a visible topographic feature of the skin surfaces and is generally the enlarged openings of pilosebaceous follicles. In this experiment, the central wavelength of 840 nm was used because the shorter wavelength improves the lateral resolution. However, our main goal was to examine the overall sebum with a higher lateral resolution. There was an insufficient amount of information about the penetration depth and photobiological effects for wavelengths longer than 1000 nm [44]. The lower wavelength of 840 nm was used to improve the lateral resolution, but it increased the scattering. By using the high-resolution OCT system, we were clearly able to resolve the fiber-rich areas due to the enhanced contrast arising from the higher scattering coefficients in the individual fiber bundle than that of the surrounding regions in the tissue. The individual fibers were more clearly visible as the numerical aperture increased. The computation was intended to determine the interior volumetric structure of the skin pore (before and after the sebum extraction). However, the scattering from the tissue medium had no impact on the results. Since the utilized wavelength was sufficient for observing the entire sebum structure with a higher transverse resolution, all the assessments were successfully conducted using 840 nm. A high numerical aperture objective lens (10× magnification) was used to increase the lateral resolution of the OCT system to assess the quantitative measurements of the biological tissue. With an improved higher resolution, the SD-OCT system provided a clearer view of the internal structure of the skin pore compared to the conventional system. Since OCT

provided the morphological information of the tissue non-invasively and dynamically, it was possible to use it as an imaging modality tool [45,46].

The acne extruder was used to extract the pore and initially, it had no impact since skin pore imaging was performed before the sebum extraction. Afterward, the pore was extracted using the acne extruder and then the imaging was taken. Since the time between the extraction and imaging of the hole was short, there was no additional tissue swelling. The extraction was done carefully so as not to affect the surface around the outer surface of the hole as our objective was to calculate the hole region as well. Throughout the experiment, the volumetric measurement of the skin pore and hole was calculated. Using the cross-sectional images, the morphological and volumetric information of the skin was acquired to analyze the skin tissue structure. The structural value is shown in Table 1. To get a 3D measurement of the internal volume, the whole surface area inside a selected length was summed together. The average surface area of the skin pore and the hole was 0.23 mm^2 (126 B-scan images) and 0.278 mm^2 (160 B-scan images) and the total volume of the skin pore and the hole was 6.28 and 9.61 mm^3, respectively. The specified images for the skin pore and the hole between 126 and 160 were chosen since the pore region before and after the sebum extraction was visible within these images. The accuracy and validity of the acquired measurement of the internal pore structure can be verified through the previous anatomical study by Lee et al. [47]. Many researchers have analyzed enlarged facial skin pores [48,49] and measured the pore surface diameter [50] and size distribution [51]. However, the methods used in each study for assessing the facial pores varied largely and there has been no volumetric measurement and analysis of the total internal volumetric structural calculation of skin pores using OCT.

As a result, we demonstrated the applicability of OCT for the morphological analysis and volumetric measure of the pore's internal volumetric structure. The obtained OCT images and data analysis played a significant role by providing quantitative structural information without dissecting the tissue region. Although the number of patients and the number of samples were limited in this study, further statistical analysis will be performed in the future. The findings of this research demonstrate that OCT can be used to analyze microscopic tissue and the valuable aspect of the non-invasive imaging capability. The notable advantages of OCT imaging that involve non-invasive and non-ionizing characteristics substantiated the feasibility of future studies, such as the monitoring and analysis of wound healing and skin treatment process.

5. Conclusions

In this study, a customized SD-OCT was used to operate as a non-destructive evaluation tool for evaluating micro-structured tissue, such as the internal volumetric structure of the skin pore. The 2D and 3D-OCT images were acquired for the initial structural assessments, while 2D-OCT images were utilized for the internal volume calculation of the skin pore before and after the sebum extraction. To enhance the lateral resolution, a high numerical aperture objective lens was used in the OCT system. In addition, to measure the internal structure of the pore without damaging the tissue, the segmentation of 2D and 3D volumetric images was performed and the algorithm for the volume measurement of the skin pore was employed. Moreover, the non-destructive, real-time OCT results precisely illustrated the potential advantages of the proposed approach over conventional histological methods. This study confirmed the feasibility of the OCT application in the pore structural analysis, and it can be concluded that the study could contribute to various future studies in tissue therapy in cosmetic fields and discover the skin elasticity that is connected with facial pore development.

Author Contributions: M.J. and J.K. designed and supervised the entire research. J.A.L., H.K. (Hyunmo Kim) and D.K. designed the optical system and performed all the experiments. J.A.L. and Y.K. provided the programming source code for the imaging. J.A.L., S.A.S. and H.K. (Hyunmo Kim) analyzed and interpreted the data. J.A.L. and S.A.S. drafted the manuscript. D.S., H.K. (Hayoung Kim) and R.E.W. helped interpret the data from a dermatological and technical point of view. M.J.

and R.E.W. critically revised the intellectual content of the manuscript. All authors have read and agreed to the published version of the manuscript.

Funding: This work was supported by the Korea Medical Device Development Fund grant funded by the Korea government (the Ministry of Science and ICT, the Ministry of Trade, Industry and Energy, the Ministry of Health & Welfare, the Ministry of Food and Drug Safety) (Project Number: RS-2020-KD000055). This research was supported by the MSIT(Ministry of Science and ICT), Korea, under the Innovative Human Resource Development for Local Intellectualization support program (IITP-2022-RS-2022-00156389) supervised by the IITP(Institute for Information & communications Technology Planning & Evaluation).

Institutional Review Board Statement: The study was conducted in accordance with the Declaration of Helsinki and was approved by the Institutional Animal and Human Care and Use Committee of Kyungpook National University (No. KNU2018-0100).

Informed Consent Statement: Informed consent was obtained from the subjects involved in the study.

Data Availability Statement: Not applicable.

Conflicts of Interest: The authors declare no conflict of interest.

References

1. Camera, E.; Ludovici, M.; Galante, M.; Sinagra, J.-L.; Picardo, M. Comprehensive analysis of the major lipid classes in sebum by rapid resolution high-performance liquid chromatography and electrospray mass spectrometry. *J. Lipid Res.* **2010**, *51*, 3377–3388. [CrossRef] [PubMed]
2. Shetage, S.S.; Traynor, M.J.; Brown, M.B.; Raji, M.; Graham-Kalio, D.; Chilcott, R.P. Effect of ethnicity, gender and age on the amount and composition of residual skin surface components derived from sebum, sweat and epidermal lipids. *Ski. Res. Technol.* **2014**, *20*, 97–107. [CrossRef]
3. Zouboulis, C.C.; Schagen, S.; Alestas, T. The sebocyte culture: A model to study the pathophysiology of the sebaceous gland in sebostasis, seborrhoea and acne. *Arch. Dermatol. Res.* **2008**, *300*, 397–413. [CrossRef] [PubMed]
4. Capitanio, B.; Lora, V.; Ludovici, M.; Sinagra, J.L.; Ottaviani, M.; Mastrofrancesco, A.; Ardigò, M.; Camera, E. Modulation of sebum oxidation and interleukin-1α levels associates with clinical improvement of mild comedonal acne. *J. Eur. Acad. Dermatol. Venereol.* **2014**, *28*, 1792–1797. [CrossRef] [PubMed]
5. Ottaviani, M.; Camera, E.; Picardo, M. Lipid mediators in acne. *Mediat. Inflamm.* **2010**, *2010*, 858176. [CrossRef]
6. Leung, A.K.; Barankin, B.; Lam, J.M.; Leong, K.F.; Hon, K.L. Dermatology: How to manage acne vulgaris. *Drugs Context* **2021**, *10*, 1–18.
7. Dong, J.; Lanoue, J.; Goldenberg, G. Enlarged facial pores: An update on treatments. *Cutis* **2016**, *98*, 33–36.
8. Maia Campos, P.M.; Melo, M.O.; Mercurio, D.G. Use of advanced imaging techniques for the characterization of oily skin. *Front. Physiol.* **2019**, *10*, 254. [CrossRef]
9. Ki, V.; Rotstein, C. Bacterial skin and soft tissue infections in adults: A review of their epidemiology, pathogenesis, diagnosis, treatment and site of care. *Can. J. Infect. Dis. Med. Microbiol.* **2008**, *19*, 173–184. [CrossRef]
10. Fritzsche, A.; Arevalo, A.; Connolly, A.; Moore, M.; Elings, V.; Wu, C. The structure and morphology of the skin of polyethersulfone ultrafiltration membranes: A comparative atomic force microscope and scanning electron microscope study. *J. Appl. Polym. Sci.* **1992**, *45*, 1945–1956. [CrossRef]
11. Sidiq, A.; Gravina, R.J.; Setunge, S.; Giustozzi, F. High-efficiency techniques and micro-structural parameters to evaluate concrete self-healing using X-ray tomography and Mercury Intrusion Porosimetry: A review. *Constr. Build. Mater.* **2020**, *252*, 119030. [CrossRef]
12. Han, W.; Zhou, G.; Gao, D.; Zhang, Z.; Wei, Z.; Wang, H.; Yang, H. Experimental analysis of the pore structure and fractal characteristics of different metamorphic coal based on mercury intrusion-nitrogen adsorption porosimetry. *Powder Technol.* **2020**, *362*, 386–398. [CrossRef]
13. Fathima, N.N.; Dhathathreyan, A.; Ramasami, T. Mercury intrusion porosimetry, nitrogen adsorption, and scanning electron microscopy analysis of pores in skin. *Biomacromolecules* **2002**, *3*, 899–904. [CrossRef] [PubMed]
14. ElHadidy, A.M.; Peldszus, S.; Van Dyke, M.I. Development of a pore construction data analysis technique for investigating pore size distribution of ultrafiltration membranes by atomic force microscopy. *J. Membr. Sci.* **2013**, *429*, 373–383. [CrossRef]
15. Sánchez-Pellicer, P.; Navarro-Moratalla, L.; Núñez-Delegido, E.; Ruzafa-Costas, B.; Agüera-Santos, J.; Navarro-López, V. Acne, Microbiome, and Probiotics: The Gut–Skin Axis. *Microorganisms* **2022**, *10*, 1303. [CrossRef] [PubMed]
16. Chilicka, K.; Rogowska, A.M.; Szyguła, R.; Rusztowicz, M.; Nowicka, D. Efficacy of oxybrasion in the treatment of acne vulgaris: A preliminary report. *J. Clin. Med.* **2022**, *11*, 3824. [CrossRef] [PubMed]
17. Chilicka, K.; Rusztowicz, M.; Rogowska, A.M.; Szyguła, R.; Asanova, B.; Nowicka, D. Efficacy of hydrogen purification and cosmetic acids in the treatment of acne vulgaris: A preliminary report. *J. Clin. Med.* **2022**, *11*, 6269. [CrossRef]

18. Landry, M.R. Thermoporometry by differential scanning calorimetry: Experimental considerations and applications. *Thermochim. Acta* **2005**, *433*, 27–50. [CrossRef]
19. Riikonen, J.; Salonen, J.; Lehto, V.-P. *Utilising Thermoporometry to Obtain New Insights into Nanostructured Materials—Review Part*; Springer: Berlin/Heidelberg, Germany, 2011.
20. Lin, S.-J.; Wu, R.-J.; Tan, H.-Y.; Lo, W.; Lin, W.-C.; Young, T.-H.; Hsu, C.-J.; Chen, J.-S.; Jee, S.-H.; Dong, C.-Y. Evaluating cutaneous photoaging by use of multiphoton fluorescence and second-harmonic generation microscopy. *Opt. Lett.* **2005**, *30*, 2275–2277. [CrossRef]
21. Calzavara-Pinton, P.; Longo, C.; Venturini, M.; Sala, R.; Pellacani, G. Reflectance confocal microscopy for in vivo skin imaging. *Photochem. Photobiol.* **2008**, *84*, 1421–1430. [CrossRef]
22. Brown, E.; McKee, T.; DiTomaso, E.; Pluen, A.; Seed, B.; Boucher, Y.; Jain, R.K. Dynamic imaging of collagen and its modulation in tumors in vivo using second-harmonic generation. *Nat. Med.* **2003**, *9*, 796–800. [CrossRef] [PubMed]
23. Huang, D.; Swanson, E.A.; Lin, C.P.; Schuman, J.S.; Stinson, W.G.; Chang, W.; Hee, M.R.; Flotte, T.; Gregory, K.; Puliafito, C.A. Optical coherence tomography. *Science* **1991**, *254*, 1178–1181. [CrossRef] [PubMed]
24. Fercher, A.F. Optical coherence tomography. *J. Biomed. Opt.* **1996**, *1*, 157–173. [CrossRef] [PubMed]
25. Mogensen, M.; Morsy, H.A.; Thrane, L.; Jemec, G.B. Morphology and epidermal thickness of normal skin imaged by optical coherence tomography. *Dermatology* **2008**, *217*, 14–20. [CrossRef] [PubMed]
26. Drexler, W.; Morgner, U.; Ghanta, R.K.; Kärtner, F.X.; Schuman, J.S.; Fujimoto, J.G. Ultrahigh-resolution ophthalmic optical coherence tomography. *Nat. Med.* **2001**, *7*, 502–507. [CrossRef]
27. Tearney, G.; Brezinski, M.; Southern, J.; Bouma, B.; Boppart, S.; Fujimoto, J. Optical biopsy in human gastrointestinal tissue using optical coherence tomography. *Am. J. Gastroenterol.* **1997**, *92*, 1800–1804.
28. Lee, J.; Saleah, S.A.; Jeon, B.; Wijesinghe, R.E.; Lee, D.-E.; Jeon, M.; Kim, J. Assessment of the Inner Surface Roughness of 3D Printed Dental Crowns via Optical Coherence Tomography Using a Roughness Quantification Algorithm. *IEEE Access* **2020**, *8*, 133854–133864. [CrossRef]
29. Shakhov, A.V.; Terentjeva, A.B.; Kamensky, V.A.; Snopova, L.B.; Gelikonov, V.M.; Feldchtein, F.I.; Sergeev, A.M. Optical coherence tomography monitoring for laser surgery of laryngeal carcinoma. *J. Surg. Oncol.* **2001**, *77*, 253–258. [CrossRef] [PubMed]
30. Lee, J.; Kim, K.; Wijesinghe, R.E.; Jeon, D.; Lee, S.H.; Jeon, M.; Jang, J.H. Decalcification using ethylenediaminetetraacetic acid for clear microstructure imaging of cochlea through optical coherence tomography. *J. Biomed. Opt.* **2016**, *21*, 081204. [CrossRef]
31. Seong, D.; Lee, C.; Jeon, M.; Kim, J. Doppler Optical Coherence Tomography for Otology Applications: From Phantom Simulation to In Vivo Experiment. *Appl. Sci.* **2021**, *11*, 5711. [CrossRef]
32. Vakoc, B.J.; Fukumura, D.; Jain, R.K.; Bouma, B.E. Cancer imaging by optical coherence tomography: Preclinical progress and clinical potential. *Nat. Rev. Cancer* **2012**, *12*, 363–368. [CrossRef] [PubMed]
33. Seong, D.; Jeon, D.; Wijesinghe, R.E.; Park, K.; Kim, H.; Lee, E.; Jeon, M.; Kim, J. Ultrahigh-Speed Spectral-Domain Optical Coherence Tomography up to 1-MHz A-Scan Rate Using Space–Time-Division Multiplexing. *IEEE Trans. Instrum. Meas.* **2021**, *70*, 1–8. [CrossRef]
34. Lee, J.; Lee, S.-Y.; Wijesinghe, R.E.; Ravichandran, N.K.; Han, S.; Kim, P.; Jeon, M.; Jung, H.-Y.; Kim, J. On-field in situ inspection for marssonina coronaria infected apple blotch based on non-invasive bio-photonic imaging module. *IEEE Access* **2019**, *7*, 148684–148691. [CrossRef]
35. Saleah, S.A.; Wijesinghe, R.E.; Lee, S.-Y.; Ravichandran, N.K.; Seong, D.; Jung, H.-Y.; Jeon, M.; Kim, J. On-field optical imaging data for the pre-identification and estimation of leaf deformities. *Sci. Data* **2022**, *9*, 698. [CrossRef] [PubMed]
36. Boppart, S.A.; Bouma, B.E.; Brezinski, M.E.; Tearney, G.J.; Fujimoto, J.G. Imaging developing neural morphology using optical coherence tomography. *J. Neurosci. Methods* **1996**, *70*, 65–72. [CrossRef] [PubMed]
37. Choi, K.S.; Wijesinghe, R.E.; Lee, C.; Lee, S.Y.; Jung, H.Y.; Jeon, M.; Kim, J. In vivo observation of metamorphosis of Plodia interpunctella Hübner using three-dimensional optical coherence tomography. *Entomol. Res.* **2017**, *47*, 256–262. [CrossRef]
38. Tripathi, S.R.; Miyata, E.; Ishai, P.B.; Kawase, K. Morphology of human sweat ducts observed by optical coherence tomography and their frequency of resonance in the terahertz frequency region. *Sci. Rep.* **2015**, *5*, 9071. [CrossRef]
39. Liu, M.; Buma, T. Biometric mapping of fingertip eccrine glands with optical coherence tomography. *IEEE Photonics Technol. Lett.* **2010**, *22*, 1677–1679. [CrossRef]
40. Potlov, A.Y.; Frolov, S.; Proskurin, S. Visualization of anatomical structures of biological tissues by optical coherence tomography with digital processing of morphological data. *Biomed. Eng.* **2020**, *54*, 9–13. [CrossRef]
41. Knuettel, A.R.; Boehlau-Godau, M. Spatially confined and temporally resolved refractive index and scattering evaluation in human skin performed with optical coherence tomography. *J. Biomed. Opt.* **2000**, *5*, 83–92. [CrossRef]
42. Ding, H.; Lu, J.Q.; Wooden, W.A.; Kragel, P.J.; Hu, X.-H. Refractive indices of human skin tissues at eight wavelengths and estimated dispersion relations between 300 and 1600 nm. *Phys. Med. Biol.* **2006**, *51*, 1479. [CrossRef] [PubMed]
43. Uhoda, E.; Piérard-Franchimont, C.; Petit, L.; Piérard, G.E. The conundrum of skin pores in dermocosmetology. *Dermatology* **2005**, *210*, 3–7. [CrossRef] [PubMed]
44. Ash, C.; Dubec, M.; Donne, K.; Bashford, T. Effect of wavelength and beam width on penetration in light-tissue interaction using computational methods. *Lasers Med. Sci.* **2017**, *32*, 1909–1918. [CrossRef]
45. Kuck, M.; Strese, H.; Alawi, S.A.; Meinke, M.C.; Fluhr, J.W.; Burbach, G.J.; Krah, M.; Sterry, W.; Lademann, J. Evaluation of optical coherence tomography as a non-invasive diagnostic tool in cutaneous wound healing. *Ski. Res. Technol.* **2014**, *20*, 1–7. [CrossRef]

46. Ghosh, B.; Mandal, M.; Mitra, P.; Chatterjee, J. Attenuation corrected-optical coherence tomography for quantitative assessment of skin wound healing and scar morphology. *J. Biophotonics* **2021**, *14*, e202000357. [CrossRef]
47. Lee, S.J.; Seok, J.; Jeong, S.Y.; Park, K.Y.; Li, K.; Seo, S.J. Facial pores: Definition, causes, and treatment options. *Dermatol. Surg.* **2016**, *42*, 277–285. [CrossRef] [PubMed]
48. Jo, H.Y.; Yu, D.S.; Oh, C.H. Quantitative research on skin pore widening using a stereoimage optical topometer and Sebutape®. *Ski. Res. Technol.* **2007**, *13*, 162–168. [CrossRef]
49. Sugata, K.; Nishijima, T.; Kitahara, T.; Takema, Y. Confocal laser microscopic imaging of conspicuous facial pores in vivo: Relation between the appearance and the internal structure of skin. *Ski. Res. Technol.* **2008**, *14*, 208–212. [CrossRef] [PubMed]
50. Wang, K.Y.; Chung, T.-S.; Gryta, M. Hydrophobic PVDF hollow fiber membranes with narrow pore size distribution and ultra-thin skin for the fresh water production through membrane distillation. *Chem. Eng. Sci.* **2008**, *63*, 2587–2594. [CrossRef]
51. Varghese, J.S.; Chellappa, N.; Fathima, N.N. Gelatin–carrageenan hydrogels: Role of pore size distribution on drug delivery process. *Colloids Surf. B Biointerfaces* **2014**, *113*, 346–351. [CrossRef]